

# ITERATIVE CT RECONSTRUCTION OF REAL DATA WITH METAL ARTIFACT REDUCTION

*Benoit Hamelin\**, *Yves Goussard\**, *David Gendron\**, *Jean-Pierre Dussault†*,  
*Guy Cloutier‡*, *Gilles Beaudoin‡* and *Gilles Soulez‡*

## ABSTRACT

We present an iterative tomographic reconstruction procedure suitable for processing of real projection datasets. This method is based on a polychromatic sinogram formation model that takes the beam hardening effect into account and thus reduces the incidence of streak artifacts due to metal inserts in the imaged body. It involves an optimized implementation and a novel measurement uncertainty model aimed at improving the conditioning of the problem and reducing the runtime of each iteration.

Reconstruction of realistic-size images was performed on both synthetic and actual projection data. Comparison with results provided by existing techniques indicates that a significant reduction of the runtime is achieved, with no loss in image quality.

**Index Terms**— Computed Tomography, Metal Artifacts, Penalized Likelihood, Real Data, Statistical Modeling.

## 1. INTRODUCTION

We take interest in the minimally-invasive measurement of the lumen of peripheral vessels that may suffer from atherosclerotic stenosis or post-angioplasty restenosis. We favor the use of X-ray CT, for its high resolution. However, the reconstructions are altered by streak artifacts because of the presence of metallic endovascular stents deployed during angioplasty. Metal screws and prosthesis may also cause such artifacts. Thus, there is a need for a reconstruction procedure that reduces metal artifacts while preserving high image resolution, for large datasets such as acquired from actual CT scanners.

In this respect, techniques based upon filtered backprojection (FBP) algorithms applied to preprocessed sinograms (such as those implemented in actual scanners) do not sufficiently reduce streak artifacts. We are then lead to an offline iterative reconstruction approach hinged on penalized likelihood maximization, such as those developed by [1, 2]. This family of reconstruction algorithms allows flexible modeling of the sinogram formation and of the statistics of projection uncertainty. Our work is based on the IMPACT algorithm developed in [1], which relies on a concise two-image polychromatic representation of the attenuating object. The IMPACT algorithm was later extended into a two-stage semi-automatic procedure that completely eliminates metal artifacts [3]. The concurrent approach [2] represents the attenuation object as a set of material mixture maps. Reconstruction is performed by maximization of the likelihood [1] or the penalized-likelihood [2] function based on identically distributed models of data uncertainties. The same model was

used in [4] for preprocessing the sinogram, taking in account multiple artifact sources.

The procedure described in [1] presents the disadvantage of a heavy computation cost when working with large images and datasets. We hereby contribute a modified reconstruction algorithm that decreases the per-iteration cost by an optimized implementation of the projection operator and a region-of-interest approach. In addition, we improve the numerical conditioning by an alternative projection uncertainty model, leading to the execution of fewer iterations to converge. On commodity hardware, the runtime of the resulting algorithm is reduced by almost one half for sinograms acquired at a normal dose, and by about one third for sinograms acquired at a lower dose.

## 2. STATISTICAL MODELS FOR SINOGRAM UNCERTAINTY

### 2.1. CT reconstruction with polyenergetic sinogram formation

The use of a polychromatic sinogram formation model is motivated by accounting for the *beam hardening* effect that leads to metal streak artifacts. When an X-ray beam traverses a strongly attenuating object (such as a metal insert), its low-energy photons have a greater absorption probability compared to its much rarer higher-energy photons. These add up to counts with significant differences from counts expected under a monochromatic source hypothesis.

This effect can be modeled by representing the object under investigation by a set of attenuation maps at  $K > 1$  energy levels. Considering the attenuation over each ray-path as a discrete Beer-Lambert integral, the discrete sinogram normalized by total photonic intensity can be expressed as  $y = \sum_{k=1}^K b_k \exp[-A\mu^k] \in \mathbb{R}^N$ . We have  $N$  the number of projection angles times the number of detectors on the array,  $\mu_k \in \mathbb{R}^{L^2}$  the vectorized  $L \times L$  attenuation map at energy level  $E_k$ ,  $b_k \in [0, 1[$  elements of a discrete approximation of the emission spectrum of the X-ray source and  $A \in \mathbb{R}^{N \times L^2}$  a fan-beam projection operator.

The difficulty related to the implied simultaneous reconstruction of  $K$  attenuation maps can be alleviated by the use of the Alvarez-Macovski decomposition of attenuation maps [1],  $\mu_k = \Phi_k\phi + \Theta_k\theta$ , with  $\phi$  mapping the attenuation due to the photo-electric effect and  $\theta$ , that due to Compton scattering. In turn, these may be empirically expressed in terms of the attenuation at a reference energy level  $\mu^0$  (namely 70 keV), so that deterministic sinogram formation may be written as

$$y = P(\mu^0) = \sum_{k=1}^K b_k \exp[-A(\Phi_k\phi(\mu^0) + \Theta_k\theta(\mu^0))]. \quad (1)$$

The number of photons that propagate through an attenuation medium is adequately modeled by a Poisson distribution that takes

\*Institut de Génie Biomédical, École Polytechnique de Montréal, Montréal, Québec, Canada.

†Département d'informatique, Faculté des Sciences, Université de Sherbrooke, Sherbrooke, Québec, Canada.

‡Centre de Recherche, Centre Hospitalier de l'Université de Montréal, Montréal, Québec, Canada.

model (1) as its parameter. The reconstruction may be seen as the penalized maximum-likelihood estimation of  $\mu^0$  and expressed as the solution to the problem

$$\min_{\mu^0 \geq 0} C_p(\mu^0) + \gamma R(\mu^0). \quad (2)$$

The first term  $C_p(\mu^0) = \sum_{i=1}^N [P_i(\mu^0) - y_i \log P_i(\mu^0)]$  enforces data adequation with respect to the log-likelihood of the Poisson distribution. The second term  $\gamma R(\mu^0)$  regularizes this ill-conditioned inverse problem using the edge-preserving  $l_2l_1$  [5] penalization of differences within pixel *cliques*. The optimization problem (2) is solved numerically. We experimented both with IMPACT [1], which we modified to take the  $l_2l_1$  regularization term in account, and with L-BFGS-B [6], a bound-constrained limited-memory quasi-Newton solver that yielded better performance.

## 2.2. Reducing the runtime

The runtime for solving problem (2) to convergence is excessive because of the necessity of executing numerous high-cost iterations, due to poor problem conditioning. Three modifications partially overcome this difficulty.

### 2.2.1. Projections and retroprojections

The fan-beam projection operator  $A$  is a matrix of dimension  $N \times L^2$ , where  $L^2$  is the total number of pixels in the image. Despite its huge size, this matrix is very sparse. We have implemented a parcimonious storage scheme for this operator that takes in account symmetries in the projection structure to store down to  $N/4$  sparse rows. Products  $Av$  and  $A^T w$  are performed using specific routines, exploiting the structure of each row or column of  $A$ , which yield runtimes lower than those obtained when using off-the-shelf tools for sparse matrix representation.

### 2.2.2. Region-of-interest framework

The actual area that we wish to image is a small square patch (of dimension about 15 cm) of the full acquired area (dimension 50 cm). However, the whole area must be considered during reconstruction, as its truncation severely compromises the conditioning of the reconstruction problem. To avoid using an attenuation map of dimension greater than 512 pixels, we represent the map using an irregular mesh, as proposed in [7]. However, this approach has two drawbacks with respect to our implementation. First, we have observed poor numerical behavior during initial reconstruction experiments with simultaneous updates of all pixels of our irregular meshes. Second, the choice of the weight  $\gamma$  of the regularization term of (2) depends on the pixel size. The calibration of these weights by manual methods is then impractical.

These shortcomings are alleviated with the ROI reconstruction framework we proposed in [8], a simplification of that in [7]. It involves the representation of the 70-keV attenuation map  $\mu^0$  by a coarse *background* image  $\mu_b^0$ , which covers the whole imaged area minus the region of interest (ROI), and by a fine *ROI* image  $\mu_r^0$ , which covers only the ROI. The linearity of the projection operator implies  $A\mu^0 \approx A_b\mu_b^0 + A_r\mu_r^0$ , with  $A_b$  and  $A_r$  being projection operators over the background and the ROI, respectively. For purposes of comparison with the scanner reconstructions, we encompass the whole imaged body in the ROI and choose its dimension as 512 pixels. This relegates only the table and the surrounding empty space to the background, which is represented as a 128-pixel map. Of course,

a ROI of smaller extent and lower dimension may be used when taking interest in small structures such as blood vessels.

The two attenuation maps are reconstructed using the alternative restriction scheme described in [8], which avoids the numerical difficulties we mentioned previously. In a nutshell, the whole imaged object is first reconstructed at coarse background resolution. The background pixels are then fixed while the ROI is reconstructed at its fine resolution. Only one regularization weight must be chosen for each map.

### 2.2.3. Alternative noise modeling

The poor conditioning of problem (2) leads us to consider a different statistical model of deviations from the deterministic sinogram. Previous works such as [9] were concerned with tomographic reconstruction under a monochromatic source hypothesis and thus sought to solve the linear system  $\tilde{y} = \log \left( y / \sum_{k=1}^K \tilde{b}_k \right) = -A\mu$ . In [9], the log-sinogram  $\tilde{y}$  is modeled as the realization of a Gaussian distribution and a reconstruction algorithm is derived from the maximization of its scaled log-likelihood.

This additive Gaussian noise model over the log-sinogram is justifiable under the assumption of large average photon counts. In that case, the Poisson distribution  $\text{Po}(P(\mu^0))$  may be approximated by the Gaussian distribution  $\text{N}(P(\mu^0), \text{diag}[P(\mu^0)])$ , so that we can write

$$y = P(\mu^0) + g,$$

with  $g \rightsquigarrow \text{N}(0, \text{diag}[P(\mu^0)])$ . Hence,

$$\tilde{y} = \log P(\mu^0) + \log (1_N + \text{diag}[P(\mu^0)]^{-1} g),$$

with  $1_N$  being a vector of  $N$  unit entries. Provided that the noise  $g$  be of low power with respect to  $P(\mu^0)$ , we have an accurate first-order approximation of the last term, so that

$$\tilde{y} \approx \log(P(\mu^0)) + \tilde{g}, \tilde{g} \rightsquigarrow \text{N}(0, R_{\tilde{g}}).$$

The reconstruction problem derived from maximizing the likelihood of  $\tilde{y}$  under this alternative uncertainty model only differs from (2) by the data adequation term, expressed as  $C_g(\mu^0) = \frac{1}{2} \|\tilde{y} - \log P(\mu^0)\|^2$ .

This noise distribution may be able to better account for the lack of precision of the deterministic sinogram model (1). Indeed, it omits multiple artifact sources such as off-focal radiation, detector effects and electronic noise [4]. Some of these are corrected through sinogram preprocessing. Yet, this preprocessing has to be taken into account explicitly, as it does not yield ideal projections with respect to model (1). Our opinion is that a Gaussian model of projection uncertainty is more robust in the face of such incompleteness of the deterministic model, as shown in section 3.2.

## 3. EXPERIMENTS AND RESULTS

In the following, we first provide simulation results regarding the convergence speed of reconstruction using the alternate uncertainty model. Second, we illustrate the feasibility of ML reconstruction of real datasets on commodity hardware, as well as the image quality increase with respect to approaches that are less runtime-intensive, such as that implemented in the scanner itself.

Due to space constraints, we will not illustrate the efficiency gained specifically through our projection operator storage, nor through the ROI framework. The former has an obvious direct impact on the per-iteration cost. The latter allows us to avoid the numerical difficulties (iteration count in excess of 2000) arising from the truncation of the reconstructed area.

### 3.1. Convergence speed assessment

We first validate the discrepancy with respect to speed of convergence between the three variants of polychromatic-source reconstruction, using a simulated projection dataset.

The numerical phantom is a simplified model of the physical phantom with metal inserts described in section 3.2. Its projections were simulated using a source spectrum model composed of  $K = 100$  energy levels. High-resolution 2048-pixel attenuation maps were derived from the material map at each energy level and their projections were added together. Noise was then incorporated into the computed sinogram to reach either a log-sinogram signal-to-noise ratio (SNR) of 35 dB or 25 dB. First, the noiseless sinogram was used as the parameter for the generation of a Poisson distribution realization; this yields a SNR of approximately 55 dB. Second, Gaussian white noise was added to the logarithm of the Poisson realization to reach the required SNR.

Reconstruction of the  $512 \times 512$  attenuation map (we don't use the ROI framework for this experiment) was stopped when the  $l_\infty$ -norm of the gradient of the objective dropped below 0.01, which represents a decrease of four to five orders of magnitude. We calibrated the regularization weight and  $l_2l_1$  threshold to obtain equivalent image quality for each dataset. Though we don't show it here due to lack of space, for both sinogram uncertainty models, the metal artifacts were eliminated, except for tiny shadows around the steel balls.

Figure 1 presents plots of the quadratic reconstruction error (with respect to the nominal 70-keV attenuation map), as well as the  $l_\infty$  norm of the gradient of the objective, over the course of the reconstructions. For the 35dB-SNR dataset, the minimization of the penalized Gaussian log-likelihood appears the most efficient: its reconstruction error has the fastest decrease, and so it is for its gradient norm (albeit its not being monotone, like IMPACT). However, for the 25dB-SNR dataset, this approach is trumped by the L-BFGS-B minimization of the penalized Poisson log-likelihood. It seems that for this dataset, the high signal-to-noise hypothesis formulated in section 2.2.3 to support an additive noise model for the log-sinogram is not satisfied. It appears that for low SNR applications, approaches based on the minimization of the Poisson log-likelihood [4] are preferable.

### 3.2. Reconstruction of real datasets

We also present the results of the reconstruction of a physical phantom acquired on a clinical scanner. The phantom was one half of an hexagonal cylinder hollowed in a circular shape. This pool was filled with agar gel that mimics the attenuating properties of soft tissues. A silicone tube was inserted into the gel pool and was filled with a water solution of iodine contrast agent at a clinical concentration. Metal balls were set near the bottom of the pool, on planes perpendicular to the cylinder axis. We reconstructed slices taken on such planes. The goal was to accurately delineate the tube of contrast agent solution.

The acquisition was performed on a Siemens SOMATOM Sensation 16 scanner, using one of two axial protocols: *SpineSeq*, designed for spine imaging, and *InnerEarSeq*, designed for inner ear imaging. The latter protocol involves a lower patient dose, so that the sinograms gathered using it have a lower SNR than those obtained using the former.

Reconstructions were performed with each algorithm used in section 3.1. We compared these to the image reconstructed by the scanner. The latter is a 512-pixel image that maps attenuation over a 14.4 cm central region. For the other three methods set in the ROI framework sketched in section 2.2.2, this region is defined as the ROI and represented samewise. The convergence criterion for these

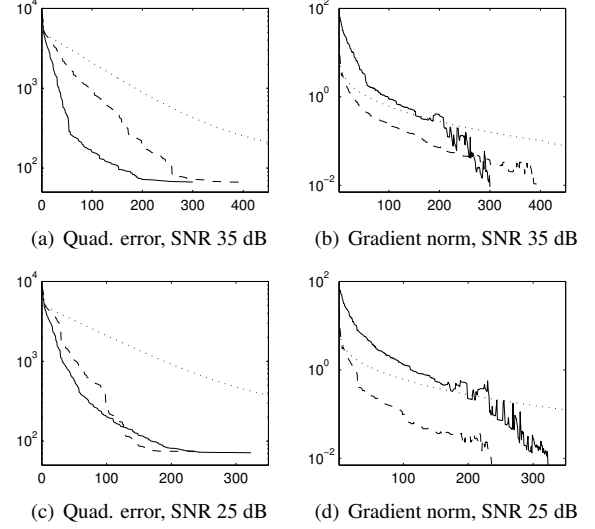


**Fig. 1.** Convergence progress for the reconstruction of simulated projections with two levels of noise. The solid line represents the L-BFGS-B minimization of the Gaussian log-likelihood; the dash line, L-BFGS-B minimization of the Poisson log-likelihood; the dotted line, the IMPACT reconstruction.

Protocol	Algorithm	Likelihood	Bkgnd (iter.)	ROI (iter.)	Runtime (min)
SpineSeq	IMPACT	Poisson	700*	700*	403
SpineSeq	L-BFGS-B	Poisson	348	225	96.2
SpineSeq	L-BFGS-B	Gaussian	117	162	49.3
InnerEarSeq	IMPACT	Poisson	700*	700*	404
InnerEarSeq	L-BFGS-B	Poisson	126	220	60.5
InnerEarSeq	L-BFGS-B	Gaussian	86	178	46.7

**Table 1.** Numerical performance, in terms of background and ROI iteration counts, and total runtime.

reconstructions, as well as their calibration, are as mentioned in section 3.1. The reconstruction is also forcibly interrupted once 700 iterations have been executed.

Figure 2 illustrates the reconstructions of the *SpineSeq* dataset (higher SNR). The tube of interest is the small grey structure under a tiny black bubble, in the middle of each image. It may be observed that metal artifacts have been reduced, but not eliminated as was reported for simulated projections. This is expected from the incompleteness of the projection model with respect to other artifact sources and data preprocessing. This aspect seems to be better tolerated under Gaussian modeling of log-sinogram noise, as streak artifacts from the metal balls appear weaker. Yet, close inspection reveals that a better delineation of the tube is obtained with both polychromatic reconstruction procedures.

Finally, Table 1 indicates the performance of each of these approaches, for each dataset. Thanks to the ROI framework, the iteration counts are reasonable (hundreds), except for IMPACT. The robustness of the Gaussian uncertainty model with respect to model inadequacy is underscored by its better performance over the *InnerEarSeq* (low SNR) dataset as well as for the background reconstructions, where the low-resolution attenuation map reduce the accuracy of the sinogram formation model. Reconstruction

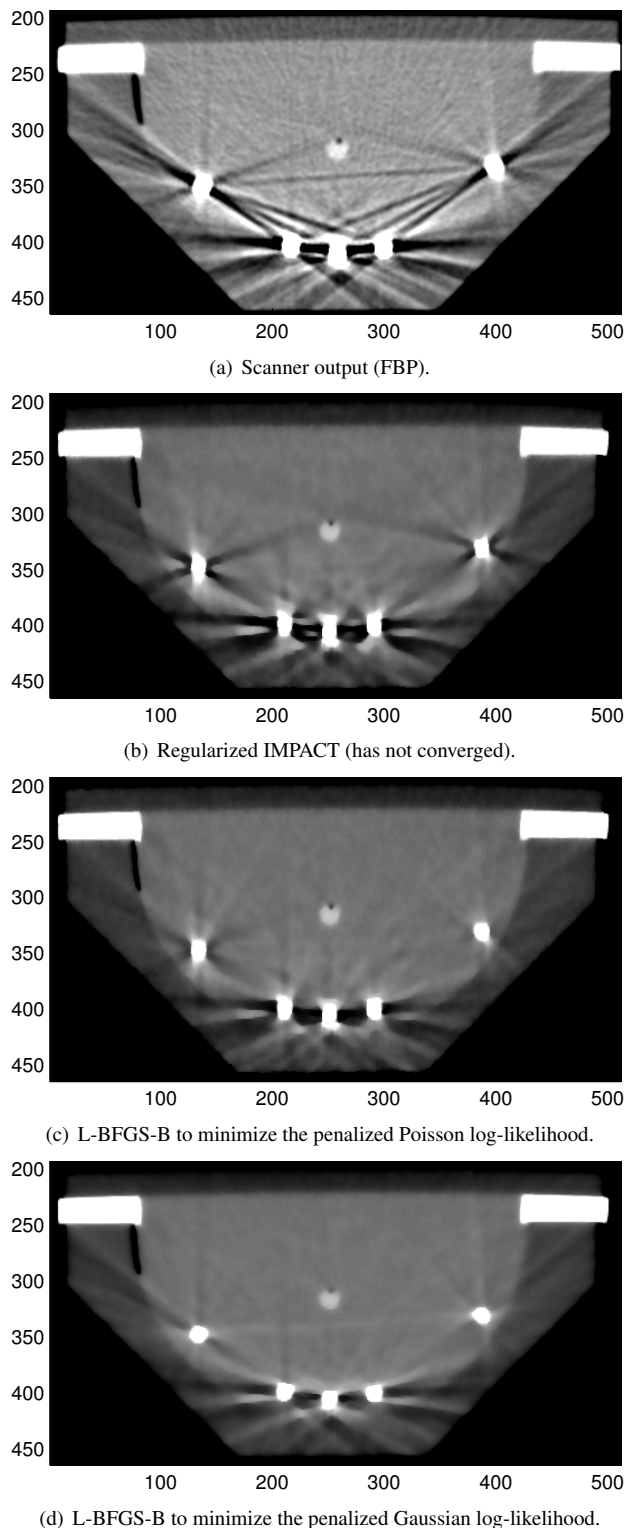


**Fig. 2.** Reconstructions of the physical phantom, scaled to a  $[-200, 200]$  HU window. The empty space around the phantom has been cropped by hand.

with Gaussian modeling of log-sinogram uncertainty yields better runtime efficiency on all accounts for both acquisition protocols.

#### 4. CONCLUSION

We have presented improvements to the modeling and the implementation for penalized-likelihood CT reconstruction with a polychromatic X-ray source model. These yield a significant decrease of the reconstruction time, for an equivalent reduction of metal artifacts. Part of this enhancement is linked to improved robustness to measurement uncertainty.

For future works, we consider the implementation of preconditioning strategies for problem (2) to further improve numerical performance. We also plan to extend our tools to 3D reconstruction, for which our ROI framework reduces the large volume of projection data to process.

**Acknowledgments** This work was funded by the Canadian Institutes of Health Research and the Natural Sciences and Engineering Research Council of Canada under Collaborative Health Research Project #323572-06.

#### 5. REFERENCES

- [1] Bruno De Man, Johan Nuyts, Patrick Dupont, Guy Marchal, and Paul Suetens, "An iterative maximum-likelihood polychromatic algorithm for CT," *IEEE Trans. Med. Imag.*, vol. 20, no. 10, 2001.
- [2] Idris A. Elbakri and Jeffrey A. Fessler, "Segmentation-free statistical image reconstruction for polyenergetic x-ray computed tomography with experimental validation," *Phys. Med. Biol.*, vol. 48, pp. 2453–2477, 2003.
- [3] Catherine Lemmens, David Faul, James Hamill, Sigrid Stroobants, and Johan Nuyts, "Suppression of metal streak artifacts in ct using a map reconstruction procedure," in *IEEE Nucl. Sci. Symp. Conf. Rec.*, 2006, pp. 3431–3437.
- [4] Patrick J. LaRivière, Junguo Bian, and Phillip A. Vargas, "Penalized-likelihood sinogram restoration for computed tomography," *IEEE Trans. Med. Imag.*, vol. 25, no. 8, pp. 1022–1036, 2006.
- [5] Pierre Charbonnier, Laure Blanc-Féraud, Gilles Aubert, and Michel Barlaud, "Deterministic edge-preserving regularization in computed imaging," *IEEE Trans. Med. Imag.*, vol. 6, no. 2, 1997.
- [6] Ciyou Zhu, Richard H. Byrd, Peihuang Lu, and Jorge Nocedal, "Algorithm 778. L-BFGS-B: Fortran subroutines for Large-Scale bound constrained optimization," *ACM Trans. Math. Soft.*, vol. 23, no. 4, pp. 550–560, 1997.
- [7] Jovan G. Brankov, Yongyi Yang, and Miles N. Wernick, "Tomographic image reconstruction based on a content-adaptive mesh model," vol. 23, no. 2, pp. 202–212, 2004.
- [8] Benoit Hamelin, Yves Goussard, and Jean-Pierre Dussault, "Penalized-likelihood region-of-interest CT reconstruction by local object supersampling," in *EMBS 2007 29th Annual International Conference*, 2007, pp. 739–742.
- [9] Charles Bouman and Ken Sauer, "A generalized gaussian image model for edge-preserving MAP estimation," *IEEE Trans. Med. Imag.*, vol. 2, no. 3, pp. 296–310, 1993.